UNIVERSITY OF AMSTERDAM

UvA-DARE (Digital Academic Repository)

Quantitative and localized spectroscopy for non-invasive bilirubinometry in neonates

Bosschaart, N.

[Link to publication](#)

CHAPTER 7

Improved acquisition speed in low-coherence spectroscopy by means of spectroscopic detection

Low-coherence spectroscopy (LCS) is a promising technique for the non-invasive determination of blood composition, but its clinical utility may be limited by the speed of the current time domain detection scheme. In this Chapter, we investigate the possibility of spectroscopic detection in LCS (sdLCS), which has a theoretical sensitivity and/or speed advantage compared to time domain detection (tdLCS).

Since sdLCS requires the acquisition of spectra with both high spectral, and high spatial resolution, a new method of acquisition and analysis was developed. In this Chapter, we validate our method computationally in a simulation and experimentally on a phantom with known optical properties. The attenuation, absorption and scattering coefficient spectra from the phantom that were measured by sdLCS agree well with the expected optical properties and are comparable to the measured optical properties by tdLCS.

7.1   Introduction

In the previous Chapters 4 to 6, we have shown that low-coherence spectroscopy (LCS) can be used to measure local absorption, scattering and backscattering coefficient spectra in turbid media over almost the complete visible wavelength range (480 to 700 nm) [1-3]. By deriving hemoglobin concentrations from absorption coefficient spectra in the dermal microcirculation (Chapter 6), we showed that LCS is a promising technique for the localized quantification of tissue chromophore concentrations, which may lead to e.g. a non-invasive alternative for invasive blood sampling [3]. However, since most clinical applications require fast measurements for instantaneous diagnosis and the reduction of motion artifacts, the measurement speed of the current time domain LCS (tdLCS) system may limit its clinical applicability. From optical coherence tomography (OCT) studies, we know that spectroscopic detection allows for more sensitive measurements compared to time domain detection [4,5], which can be exchanged for higher acquisition speed at unaltered sensitivity. Therefore, in this Chapter we investigate the possibility for spectroscopic detection in LCS (sdLCS), focusing primarily on validating a new method of analysis that was developed for this purpose.

Spectroscopic detection in OCT commonly involves spectrographs with high spectral resolution, a narrow wavelength range and a large number of pixels, resulting in large effective imaging depths (i.e. high maximal imaging depth and weak sensitivity roll-off in depth). Consequently, an A-scan of several mm can be recovered from a single back scattered spectrum, which is used for constructing an intensity image with high spatial resolution [4,5]. In LCS, we are mainly interested in the spectral content of the signal within a confined volume and hence, LCS requires both high spatial and sufficient spectral resolution (Chapter 4). In the case of spectroscopic detection, this can be achieved either by signal processing after acquisition [6], or by adjusting the signal acquisition itself. Since the latter has not been investigated before, we developed a new approach for signal acquisition in sdLCS.

Our approach involves step-wise detection of local back scattered spectra with a spectrograph that has an effective imaging depth of only 9 μm in air. Thereby, we achieve both high spatial and sufficient spectral resolution (6 nm) and we maintain the advantage of focus tracking, as we had in our tdLCS system. The main challenge in step-wise spectroscopic detection with limited imaging depth involves removing the mirror image that originates from the complex ambiguity of the LCS signal. Methods for mirror image removal in OCT imaging commonly involve phase modulation and filtering of the modulated signal [8-10]. Similarly, our approach is to modulate the LCS signal, by using an oscillating mirror in the reference arm.

Since the primary aim of this Chapter is to validate whether we can use this new approach for the determination of local absorption and scattering coefficient spectra, we will provide proof of principle with an on-the-shelf spectrograph (USB4000, Ocean Optics, USA). Only part of the feasible speed advantage is demonstrated, since the quantum efficiency and acquisition speed of this spectrograph are not optimized for sdLCS. After describing the theory behind sdLCS, we will validate our algorithm with a simulation of an sdLCS absorption measurement, while simulating the USB4000 as the detecting spectrograph. Subsequently, we experimentally demonstrate the ability of

sdLCS to measure the attenuation, absorption and scattering coefficient spectra from a polystyrene-dye phantom, and we compare our results to a tdLCS measurement.

7.2 Theory

The main difference between sdLCS and tdLCS, is that the detector current i_D is acquired as a function of wavelength λ (e.g. by a spectrograph), instead of time by a photodiode (Chapters 4 to 6). Similar Eq. 4.1 for tdLCS, i_D is modulated by the path length difference between the sample arm and the reference arm $\Delta L = 2(x_S - x_R)$, with sample arm length x_S and reference arm length x_R. Hence, for sdLCS we can write:

$$i_D(k) \propto I_S(k) + I_R(k) + \sqrt{I_S(k) \cdot I_R(k)} \cdot 2\cos(k\Delta L) \tag{7.1}$$

where k is the wavenumber ($k = 2\pi/\lambda$) and I_S and I_R are the signal intensities in the sample and reference arm, respectively. The two left terms of Eq. 7.1 denote the ('DC') non-modulated part of $i_D(k)$ and the right term denotes the ('AC') modulated part of $i_D(k)$, as has been illustrated in Figure 7.1a. Since I_S and I_R both originate from the source spectrum S_0, the modulation term in Eq. 7.1 can be written in terms of S_0. In case of a single reflector at path length ℓ (depth $\ell/2$), this results in:

$$i_{D,modulated}(k) \propto \sqrt{\eta_S \cdot \eta_R \cdot e^{-\mu_t\ell}} \cdot S_0(k) \cdot 2\cos(k\Delta L) \tag{7.2}$$

with η_S and $\eta_R = 1 - \eta_S$ the fractions of S_0 that are guided towards the sample and reference arm, respectively, as determined by the splitting ratio of the beam splitter. The light originating from the sample arm is backscattered by a sample with an attenuation coefficient μ_t and hence, I_S is attenuated by Beer's law if the geometrical path length ℓ in the sample increases. In sdOCT, an A-scan (i.e. the backscattered intensity as a function of $d = \frac{1}{2}\Delta L$) is obtained by Fourier transformation of $i_D(k)$:

$$i_D(\Delta L) = \left| \Im\{i_D(k)\} \right|^2 \tag{7.3}$$

As illustrated in Figure 7.1b, the horizontal axis of $i_D(\Delta L)$ runs from $-\Delta L_{max}$ to ΔL_{max}. For every ΔL a 'mirror image' is present at $-\Delta L$, i.e. both these path length differences result in the same modulation frequency on $i_D(k)$ (Eq. 7.1 and 7.2). The Nyquist criterion defines the maximal measurable path length difference ΔL_{max}, or imaging depth $d_{max} = \frac{1}{2}\Delta L_{max}$:

$$\Delta L_{max} = \frac{\pi}{\delta k} \tag{7.4}$$

in which $\delta k = (k_{max} - k_{min})/N_p$ depends entirely on the properties of the detecting spectrograph, which are the number of pixels N_p, and the minimal and maximal detectable wave number k_{min} and k_{max}.

The path length range over which $I(\Delta L)$ can be observed not only depends on ΔL_{max}, but also on the sensitivity roll-off with ΔL of the spectrograph, caused by the finite spectrometer resolution [11]:

$$I(\Delta L) = \frac{\sin^2\left(\pi\Delta L / 2\Delta L_{max}\right)}{\left(\pi\Delta L / 2\Delta L_{max}\right)^2} \cdot \exp\left(-\frac{\pi^2\left(\Delta k / \delta k\right)^2}{8\ln 2}\left(\frac{\Delta L}{\Delta L_{max}}\right)^2\right) \tag{7.5}$$

in which Δk is the spectral resolution of the spectrograph.

Since we use sdLCS for doing spectroscopy, we are interested in the spectrum $i_D(k)$ itself, rather than an A-scan as in sdOCT. However, Eq. 7.4 and 7.5 are important for sdLCS, since the ΔL_{max} and the signal roll-off determine the highest measurable modulation frequency in $i_D(k)$, and therefore the spatial resolution at which the spectrum $i_D(k)$ can be acquired. In contrast to sdOCT, sdLCS requires low values of ΔL_{max} and a fast sensitivity roll-off to obtain good spatial resolution for $i_D(k)$ (see Section 7.4). Similar to tdLCS, this introduces a trade-off between the spectral and spatial resolution of $i_D(k)$, because a fast sensitivity roll-off is accompanied by a low spectral resolution Δk (Eq. 7.5).

7.2.1   *Mirror image removal*

Merely acquiring $i_D(k)$ within a confined path length range does not provide us with a spectrum that we can use for the determination of μ_t, since $i_D(k)$ contains unwanted DC (i.e. non-modulated components) and modulation components (Eq. 7.1 and 7.2). Moreover, the mirror image induces cross-talk between $i_D(\Delta L)$ and $i_D(-\Delta L)$ within the investigated path length range. This complex ambiguity can be removed by phase modulation and frequency domain filtering of the signal. Therefore, we modulate $i_D(k)$ using the oscillating mirror in the reference arm of our LCS system, which introduces a Doppler shift f_D to the signal:

$$f_D = \frac{2v_R}{\lambda} = \frac{v_R \cdot k}{\pi} \tag{7.6}$$

with v_R the velocity of the reference mirror. Acquisition of N spectra $i_D(k)$ at every integration time τ of the spectrograph results in a dataset $i_D(k,t)$, as illustrated in Figure 7.1c. The phase of the modulation on $i_D(k,t)$ changes at every τ, because the movement of the reference mirror induces a change in ΔL (vertical direction in Figure 7.1c). Figure 7.1d illustrates the time-modulation on $i_D(k,t)$ by f_D for one wavelength (horizontal direction in Figure 7.1c). Since the sensitivity of the measurment is largest around $\Delta L = 0$ or 'zero delay' (Eq. 7.5), the range of ΔL is chosen such that it crosses zero delay at $\frac{1}{2}N\tau$ (Figure 7.1e). The integration time of the spectrograph should be chosen such that the time-modulation on $i_D(k,t)$ is adequately sampled. Hence the sampling frequency $f_s = 1/\tau$ needs to be larger than $2f_{D,max}$ (the largest value of f_D within the investigated spectral range). For the integration time, this results in:

$$\tau < \frac{\pi}{2v_R \cdot k_{max}} = \frac{\lambda_{min}}{4v_R} \tag{7.7}$$

with k_{max} the largest wave number and λ_{min} the shortest wavelength within the investigated spectral range.

Fourier transformation on $i_D(k,t)$ with respect to t provides the frequency content of the signal $i_D(k,f)$, which contains the modulation frequency f_D, its mirror image and a DC component (Figure 7.1f). By filtering out the part of $i_D(k,f)$ containing only the positive

frequencies $+f_D$, the unwanted DC component and the negative frequencies $-f_D$ are lost. Now that $i_D(k)$ is confined both in amplitude and phase, the complex ambiguity and the mirror image in the path length domain (Figure 7.1b) are lost. Inverse Fourier transformation on the filtered $i_D(k,f)$ with respect to f provides a smooth, non-modulated $i_D(k,t)$ (Figure 7.1g), and averaging of $i_D(k,t)$ over time results in the final spectrum **S** that we can use for the determination of μ_t (Figure 7.1h).

Similar to tdLCS, a dataset $S(\ell)$ is generated by step-wise alteration of the depth or geometrical round trip path length ℓ in the sample around which $i_D(k)$ is acquired (Chapter 4). Hence, the advantage of focus tracking that we had in tdLCS can still be applied in sdLCS.

7.2.2   *Sensitivity and/or speed advantage*

Our method for sdLCS provides a sensitivity advantage over tdLCS, which can be explained in terms of the signal to noise ratio (SNR). The SNR of any shot-noise limited LCS system is given by:

$$\textbf{SNR} = \frac{\boldsymbol{\varepsilon}\cdot\textbf{S}}{h\boldsymbol{v}\cdot\Delta f} \tag{7.8}$$

in which $\boldsymbol{\varepsilon}$ is the detection efficiency, $h\boldsymbol{v}$ the photon energy and Δf the detection bandwidth of the system [5]. Using Eq. 4.8, we can write:

$$\Delta f = 2f_{scan}d_{scan}\frac{\Delta\lambda}{\lambda_0^2} \tag{7.9}$$

with f_{scan} the scan rate and d_{scan} the scan length for the acquisition of one spectrum. For tdLCS, $f_{scan}=2f_R$ and $d_{scan}=\Delta R$ (Chapter 4). For sdLCS, $f_{scan}=1/\tau$ and $d_{scan}=2d_{max}=\Delta L_{max}=\lambda^2/(2\delta\lambda)$, if mirror image removal is applied. If we assume that in sdLCS, N_p pixels cover the bandwidth of the spectrum **S**, i.e. $N_p\cdot\delta\lambda=\Delta\lambda$, then d_{scan} can be written into $d_{scan}= N_p\lambda^2/2\Delta\lambda$. Hence for sdLCS, Δf reduces to $\Delta f=N_p/f_{scan}$. As a consequence, the SNR of a tdLCS system compares to the SNR of an sdLCS system as $SNR_{TD} = (\boldsymbol{\varepsilon}\cdot\textbf{S})/(h\boldsymbol{v}\cdot\Delta f) = (\tau\cdot\boldsymbol{\varepsilon}\cdot\textbf{S})/(h\boldsymbol{v}\cdot N_p) = SNR_{SD}/N_p$. In conclusion, sdLCS is N_p-times more sensitive than tdLCS, provided that both systems have the same f_{scan}, d_{scan} and $\boldsymbol{\varepsilon}$. This sensitivity advantage can be exchanged for a speed advantage if f_{scan} is increased, i.e. an sdLCS system can measure N_p-times faster than a tdLCS system with equal sensitivity.

A change in f_{scan} – i.e. between a 'fast' and a 'slow' LCS system – results in an SNR change with a factor $\varphi=\Delta f_{slow}/\Delta f_{fast}=(f_{scan,slow}d_{scan,slow})/(f_{scan,fast}d_{scan,fast})$, which comprises $\varphi=2f_R\tau(\Delta R/\Delta L_{max})$ for a 'fast' system with the sdLCS settings (but without spectral detection) and a 'slow' system with the tdLCS settings. If in addition, spectral detection over N_p pixels is realized for the 'fast' system (as for our sdLCS system), the SNR will increase with a factor N_p. As a consequence, the SNR_{SD} of an sdLCS system relates to the SNR_{TD} of a tdLCS system as:

$$\textbf{SNR}_{\textbf{SD}} = \varphi\cdot N_p\cdot\frac{\boldsymbol{\varepsilon_{SD}}}{\boldsymbol{\varepsilon_{TD}}}\cdot\textbf{SNR}_{\textbf{TD}} = 2f_R\cdot\tau\cdot N\cdot\frac{\boldsymbol{\varepsilon_{SD}}}{\boldsymbol{\varepsilon_{TD}}}\cdot\frac{\Delta R}{\Delta L_{max}}\cdot\textbf{SNR}_{\textbf{TD}} \tag{7.10}$$

which also considers a possible difference in detection efficiency between sdLCS and tdLCS.
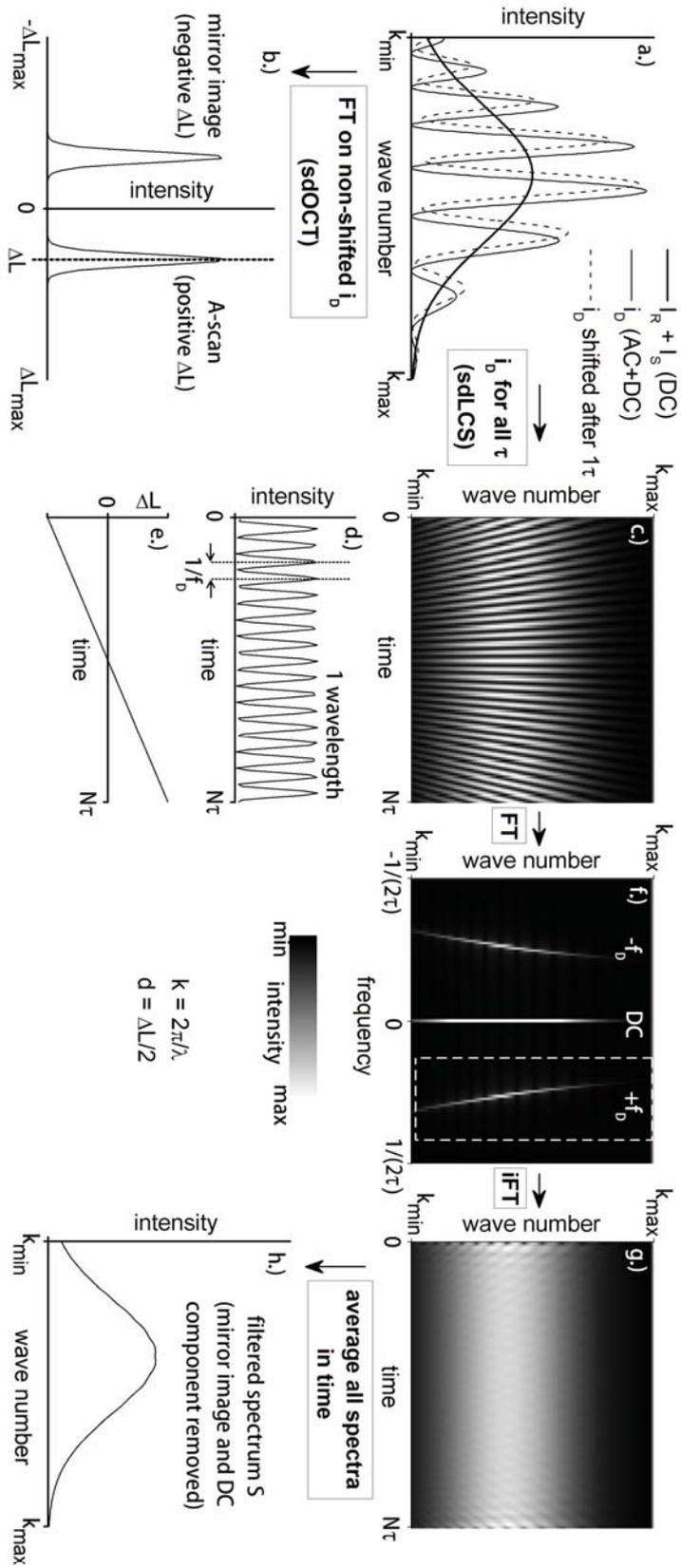
Figure 7.1 *Signal acquisition and processing in sdLCS. See Section 7.2 for details.*

7.3   Simulation

In order to validate the data acquisition and analysis approach described in Section 7.2, we simulated an absorption measurement on a sample containing oxyhemoglobin [12]. Since scattering was neglected in the simulation, the attenuation coefficient μ_t in Eq. 7.2 can be simplified to the absorption coefficient μ_a. The spectrum $S(\ell)$ was calculated at ℓ_1 = 2 mm and ℓ_2 = 4 mm inside the sample, corresponding to depths d_1 = 1 mm and at d_2 = 2 mm, respectively.

The detecting spectrograph was simulated with the properties of the USB4000 (λ_{min} = 345 nm, λ_{max} = 1042 nm, N_p = 3648). The integration time was set at the minimal integration time of the USB4000 for these measurements, τ = 6 ms. To meet the requirement in Eq. 7.7, the velocity of the reference mirror was set at v_R = 6 μm/s (frequency f_R = 0.3 Hz, amplitude ΔR = 20 μm). The source spectrum S_0 was simulated as a Gaussian with center wavelength λ_0 = 550 nm and bandwidth λ_{FWHM} = 140 nm. The sample arm fraction was η_S = 0.1, resulting in a reference arm fraction of η_R = 0.9. A total number of N = 125 spectra was acquired over a time interval of $N\tau$ = 0.75 s. The initial ΔL was set at -4.5 μm to achieve zero delay at ½Nτ.

Figure 7.2 shows the result of this simulation. The $i_D(\lambda)$ at ℓ_1 and ℓ_2 show little influence of the sample's absorption (Figure 7.2a). However, after phase modulation and frequency domain filtering of $i_D(\lambda)$, the resulting spectra S at ℓ_1 and ℓ_2 clearly show the presence of the oxyhemoglobin absorption peaks (Figure 7.2b). Using Beer's law, we obtain the absorption coefficient of the sample:

$$\mu_a = -\frac{1}{\frac{1}{2}(\ell_2 - \ell_1)} \ln\left(\frac{S(\ell_2)}{S(\ell_1)}\right) \tag{7.11}$$

From Figure 7.2c, we can conclude that our method of data acquisition and analysis for sdLCS fully recovers the input μ_a of this simulation.
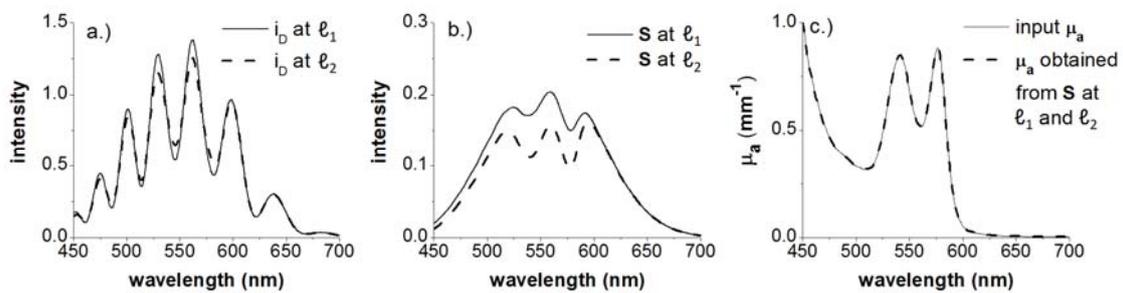

Figure 7.2 *Simulation of a μ_a measurement in sdLCS. a.) input spectra i_D and b.) filtered spectra S at path lengths ℓ_1 and ℓ_2 inside the sample. c.) input μ_a and recovered μ_a from Eq. 7.8.*

7.4 The path length window Δℓ in sdLCS

In sdLCS, the path length window over which **S**(ℓ) is acquired depends not only on the reference mirror scanning window in the medium (Δℓ$_R$ = 2ΔR/n$_g$ = 30 μm with the settings of Section 7.3 and group refractive index n$_g$ = 1.35), but also on the path length window that is probed by the spectrograph Δℓ$_S$. The latter is a combination of 2ΔL$_{max}$ (due to mirror image removal) and the sensitivity roll-off with ΔL of the spectrograph. For the USB4000, we can calculate that 2ΔL$_{max}$ = 1880 μm (Eq. 7.4), but its sensitivity roll-off is not readily available.

To determine the sensitivity roll-off of the USB4000, we both calculated (Eq. 7.5) and measured its roll-off function. Since the only unknown parameter in Eq. 7.5 is the spectral resolution Δk (or Δλ = 2π/Δk), we measured Δλ = 6 nm as the FWHM of a 543 nm and 633 nm HeNe laser line, projected on the spectrograph. This spectral resolution results in a theoretical sensitivity roll-off with a FWHM of 18 μm, indicated by the dotted line in Figure 7.3.

We experimentally determined the sensitivity roll-off by measuring the reflection from a glass slide in the sample arm as a function of ΔL between the sample arm and the reference arm, using Eq. 7.3. The measured i$_D$(λ) was resampled to a linear k-scale. The resulting sensitivity roll-off function is shown in Figure 7.3 and agrees very well with the theoretical function. Note that the width (FWHM) of the reflections at each value of ΔL is close to twice the coherence length (2·l$_c$ ≈ 3 μm, Eq. 4.4) of the source (identical to the source in Chapters 4 to 6), and therefore agrees with the theoretical resolution for ΔL.

Since the FWHM of the sensitivity roll-off of the USB4000 is 18 μm, which is many times smaller than the 2ΔL$_{max}$ of 1880 μm, the path length window that is probed by the USB4000 can be approximated with Δℓ$_S$ = 18/n$_g$ = 13 μm. This Δℓ$_S$ probes a path length window around every path length ℓ in the reference mirror scanning window Δℓ$_R$. Hence, the full path length window that is probed in sdLCS is a convolution of Δℓ$_R$ with Δℓ$_S$, resulting in Δℓ = Δℓ$_R$ + Δℓ$_S$ = 30 + 13 = 43 μm (inset of Figure 7.3).
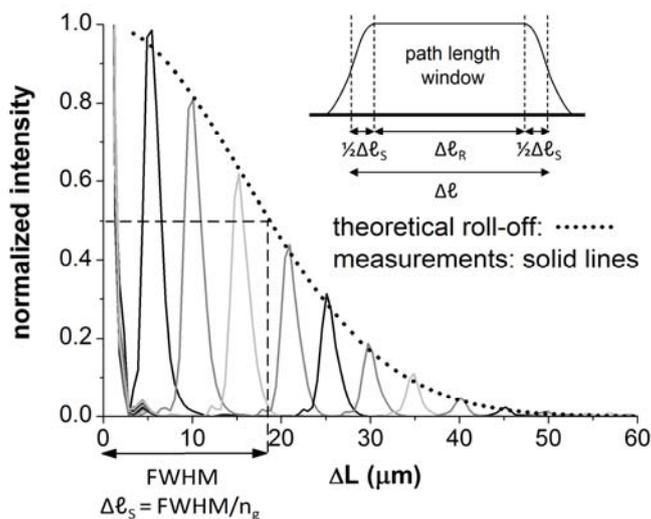

Figure 7.3 *Theoretical and measured sensitivity roll-off of the USB4000. Inset: illustration of the path length window Δℓ in sdLCS.*

7.5   Experimental validation – Methods

To experimentally validate our approach for sdLCS (Section 7.2), we measured attenuation spectra μ_t from 480 to 700 nm on a phantom with known absorption μ_a and scattering μ_s coefficient spectra and we separated the individual contributions of μ_a and μ_s from the measured μ_t. In addition, we compared our sdLCS results to the results of a tdLCS measurement on the same phantom with the tdLCS system described in Chapters 4 to 6 (Figure 4.1) [1-3].

Table 7.1 *Acquisition settings for sdLCS and tdLCS*

acquisition parameter	sdLCS	tdLCS
$\Delta\ell$	43 µm	44 µm
$\Delta\lambda$	6 nm (all λ)	4 nm @ λ=480 nm 9 nm @ λ=700 nm
v_R	0.006 mm/s	1.84 mm/s
f_R	0.3 Hz	23 Hz
ΔR	20 µm	40 µm
N = # averages per ℓ	250	250
acquisition time of $S(\ell)$	$N\tau$ = 1.5 s	$N/(2f_R)$ = 5.4 s

7.5.1   System and acquisition

The sdLCS system described in this Chapter is identical to the tdLCS system in Chapters 4 to 6, except for the detection end of the system, which consists of a spectrograph rather than a photodiode/lock-in amplifier combination. Hence, the multimode detection fiber is connected to the detecting spectrograph (USB4000), from which the properties have been described in Section 7.3.

For both the sdLCS and tdLCS measurements, we controlled ℓ (ℓ = 0 – 2000 µm) by translating the reference mirror in steps of 27 µm. By translating the sample in the axial direction, focus tracking of the spot size (r = 4.5 µm) in the medium was achieved. At every ℓ, back scattered power spectra $S(\ell)$ were obtained over a path length window in the medium of $\Delta\ell$ = 43 µm for sdLCS (see Sections 7.2 and 7.4) and $\Delta\ell$ = 44 µm for tdLCS (see Chapter 4). For both sdLCS and tdLCS, $S(\ell)$ was temporally averaged (N = 250 spectra per ℓ) and corrected for the background (i.e. the LCS spectrum obtained from the non-scattering glass of the inner cuvette wall of the sample). The integration time for the sdLCS measurements was set at τ = 6 ms and the reference mirror velocity at v_R = 6 µm/s, identical to the settings of the simulation (Section 7.3). The acquisition

settings for the tdLCS measurements were identical to the settings in Chapters 4 to 6 [1-3]. For both sdLCS and tdLCS, the most important acquisition parameters have been summarized in Table 7.1. Note that the acquisition speed for one temporally averaged spectrum $S(\ell)$ is 3.6 times faster for sdLCS.

Similar to the data analysis in Chapters 4 to 6, fitting the single exponential decay model $S(\ell)= \alpha \cdot \exp(-\mu_t \cdot \ell)$ (free running fit parameters α and μ_t) to the sdLCS and tdLCS acquired $S(\ell)$ vs. ℓ, results in a μ_t spectrum for both detection methods [1-3]. Uncertainties in α and μ_t are estimated by their 95% confidence intervals (c.i.). Since the spectral resolution in sdLCS ($\Delta\lambda$ = 6 nm, Section 7.4) is higher than the pixel width of 0.2 nm, $S(\ell)$ was binned into wavelength regions of 6 nm for the sdLCS measurements. The values of μ_a and μ_s were obtained by fitting their individual contributions to the measured μ_t, as described in Chapter 6.2.2 [3].

7.5.2   *Phantom*

We prepared one phantom, consisting of 0.096 vol% NIST-certified polystyrene spheres (Ø 602±6 nm, Thermo Scientific, USA) and 10% magenta dye (Ecoline #337, Royal Talens, The Netherlands). The μ_s of the polystyrene spheres was calculated using Mie theory and integrated over the size distribution of the spheres (2*SD), as described in Chapter 5.2.4 [2]. The μ_a of the dye was determined in a separate transmission measurement on the dye only, as described in Chapter 4.3.2 [1]. For the tdLCS measurements, both reference spectra for μ_s and μ_a were convolved with a Lorentzian with a line width of 9 nm for adequate comparison to the LCS spectra that are Doppler broadened by Brownian motion (Chapters 4 to 6) [1-3]. For the sdLCS measurements, Brownian motion does not induce spectral broadening, because the Doppler shifted frequencies are still within the bounds of the frequency domain filter (Figure 7.1f). Since the reference spectrum of μ_s was obtained with the same spectral resolution as the LCS spectra, we did not broaden this spectrum. The reference spectrum of μ_s was convolved with a Lorentzian with a line width of 6 nm ($\Delta\lambda$ of the USB4000).

7.5.3   *SNR comparison of sdLCS and tdLCS*

In order to compare the sensitivity of the current sdLCS system to the tdLCS system, we measured the SNR of the two detection methods, using a mirror in the sample arm. The optical powers in the sample and reference arm were equal and the acquisition settings in Table 7.1 were applied. For both sdLCS and tdLCS, the spectrally resolved SNR was determined from the measured spectrum S using:

$$\mathbf{SNR} = 10 \cdot \log\left(\frac{\mathbf{S}}{\text{var(noise)}}\right) \tag{7.12}$$

and normalized to zero SNR. In Eq. 7.12 var(noise) denotes the variance of the noise floor in S for both methods, determined in the wavelength region between 310 and 385 nm where no signal was expected.

Based on Eq. 7.10, we can calculate the expected difference in SNR between both systems. The LCS spectrum covers approximately N_p=1150 pixels on the USB4000. Based on a maximum number of 4.10^6 counts per photon and a pixel well depth of 1.10^5 electrons, the quantum efficiency (QE = #electrons/photon) of the USB4000 is 2.5% at 600 nm. Using the photodiode response of 0.43 A/W (2001, New Focus, USA), we can

calculate that our tdLCS detector has a QE of 89% at 600 nm. With τ=6 ms for our sdLCS system, the sensitivity advantage of the sdLCS measurements described in this Chapter reduces to 0.38. Hence, when using the USB4000 as a detector for sdLCS and the settings in Table 7.1, we can expect a decrease in SNR of 4.2 dB at 600 nm with respect to tdLCS.
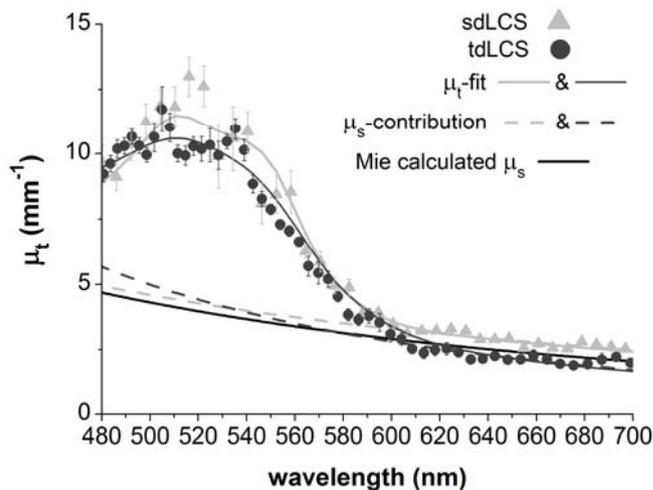

Figure 7.4 *Comparison of an sdLCS measurement to a tdLCS measurement of μ_t, μ_a and μ_s on a polystyrene-dye phantom.*
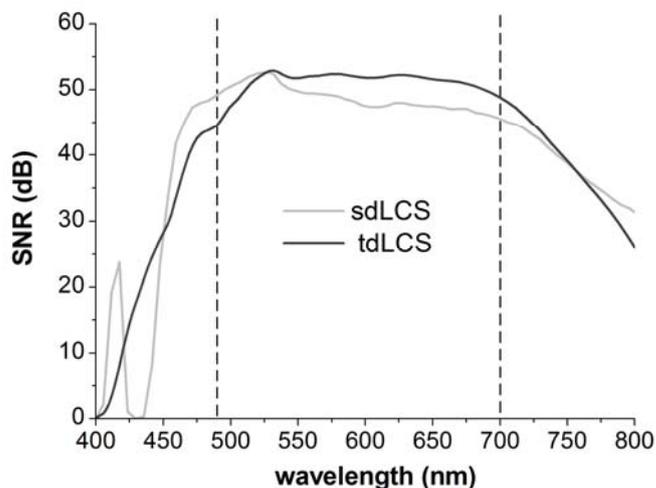

Figure 7.5 *Signal to noise ratio (SNR) in sdLCS and tdLCS. The investigated spectral range for the measurements in this Chapter runs from 480 to 700 nm (dashed lines).*

7.6   Experimental validation – Results

Figure 7.4 shows the measured μ_t spectra by sdLCS and tdLCS on the polystyrene-dye phantom. The μ_t spectra from both detection methods agree within the estimated uncertainties (error bars) for nearly all wavelengths. Also the fits on μ_t and the μ_s-contributions to the fits agree well, and the μ_s-contributions are in good agreement

with the Mie calculated $\mathbf{\mu_s}$. The fitted dye concentrations were 10.1 ± 0.4% for the sdLCS measurement and 9.5 ± 0.4% for the tdLCS measurement, which are both very close to the expected dye concentration of 10%.

Figure 7.5 shows the measured SNR on a mirror. For both sdLCS and tdLCS, the SNR is maximal within the investigated spectral range of 480 to 700 nm. For the majority of wavelengths within this region, the SNR of tdLCS is larger than the SNR of sdLCS, except for the shortest wavelengths (λ < 530 nm). The decrease in SNR for sdLCS is close to the predicted value of –4.2 dB (Section 7.5.3). Note that the SNR value for tdLCS differs from the value given in Chapter 4 (112 dB) due to a difference in method of analysis. Whereas the SNR in Chapter 4 describes the minimally detectable signal with maximal amplification by the lock-in amplifier, the SNR in this Chapter is obtained with detection settings closer to actual measurements (e.g. with a backscatter coefficient larger than the minimal detectable reflectivity). However, the quantitative value of the SNR is of less importance here, since we primarily consider the differences in SNR in Figure 7.5 for the comparison between sdLCS and tdLCS.
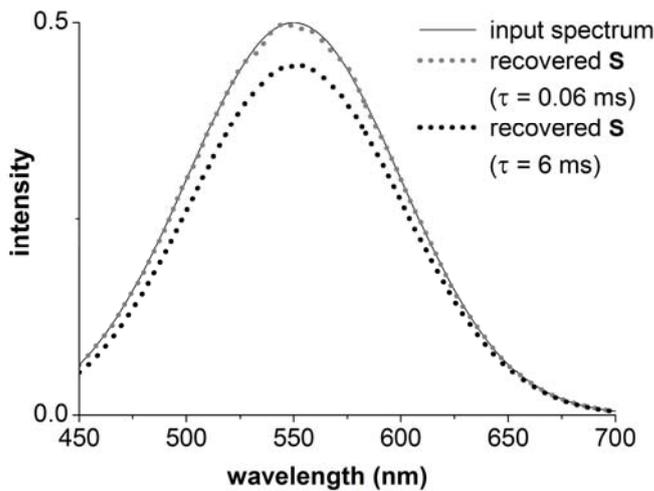

Figure 7.6 Simulation of the recovered spectrum S for two integration times: τ = 0.06 ms (with v_R = 60 μm/s) and τ = 6 ms (with v_R = 6 μm/s).

7.7   Discussion and conclusion

In this Chapter, we demonstrated and validated a new detection method and analysis algorithm for spectroscopic detection in LCS. We showed that this method can be used for measuring local $\mathbf{\mu_t}$, $\mathbf{\mu_a}$ and $\mathbf{\mu_s}$ spectra in turbid media. The results of the sdLCS phantom measurement agreed well with the expected optical properties of the phantom and were comparable to the measured optical properties by tdLCS (Figure 7.4).

The reason to validate this new detection method, is its theoretical sensitivity advantage compared to time domain detection (Section 7.2.2). As a consequence, the acquisition speed of the measurement can be reduced with respect to time domain detection, without reducing the signal to noise ratio. The sdLCS system that was

validated in this Chapter was more than three times faster than the tdLCS system, but not more sensitive (Figure 7.5). A sensitivity advantage for sdLCS could not be demonstrated, because the quantum efficiency of the USB4000 is not optimized for these experiments. However, if the quantum efficiency would be similar to that of our tdLCS detector, the sensitivity advantage would be $10\log(\phi N_p) = 11$ dB at equal acquisition times for tdLCS and sdLCS (Section 7.5.3).

Figure 7.5 shows a decrease in SNR of approximately 5 dB for sdLCS compared to tdLCS, which is slightly lower than the predicted decrease of 4.2 dB (Section 7.5.3) for these detection settings. The additional decrease in sensitivity can be explained by the relatively slow acquisition speed (167 Hz) of the USB4000. Slow acquisition speeds result in a decrease of the modulation depth in $i_D(\lambda)$ ('fringe wash-out'), due to the reference mirror movement induced change of ΔL within the integration time. Hence, the sensitivity of our sdLCS measurements can be improved by increasing the integration time with respect to the velocity of the reference mirror. The effect of fringe wash-out on spectral amplitude has been illustrated in Figure 7.6. Comparable to the simulation in Section 7.3, Figure 7.6 shows the recovered spectra **S** from a simulation without absorption using integration times of $\tau = 6$ ms and $\tau = 0.06$ ms and reference mirror velocities of 6 µm/s and 60 µm/s, respectively. Note that the integration times differ two orders of magnitude, whereas the reference mirror velocities only differ one order of magnitude. As a consequence, the spectrum **S** for $\tau = 0.06$ ms has a higher amplitude (±15%, corresponding to 0.6 dB) and shows better agreement with the input sample arm spectrum ($\eta_S \cdot S_0$) than the spectrum **S** for $\tau = 6$ ms. This simulation shows that, besides improvements on quantum efficiency, a faster spectrograph will further improve the performance of our sdLCS system. Since high quantum efficiency line scan cameras are available with line rates up to 140 kHz (e.g. the Basler Sprint spL4096-140km, Basler AG, Germany), enhanced sensitivity and/or acquisition speed are realizable for sdLCS.

The only technique that is reported to have comparable performance to our sdLCS system in terms of localized measurements of optical properties, is dual band sOCT [6,7]. However, this method may not be as well applicable on thin layers or small tissue volumes as our LCS system [3], since the spatial dimensions of the largest of the dual bands in this method may extend the dimensions of the volume of interest. In addition, our sdLCS system has the unique advantage of focus tracking, which prevents unwanted signal attenuation and a decrease in sensitivity at larger path lengths in the medium. This facilitates the exact determination of $\boldsymbol{\mu_s}$ and $\boldsymbol{\mu_a}$ contributions to the measured $\boldsymbol{\mu_t}$.

In conclusion, the new approach for sdLCS demonstrated in this Chapter has high potential to improve the accuracy and speed of localized optical property measurements by LCS. Undoubtedly, this will lead to improved clinical utility of the technique, e.g. for the non-invasive determination of blood composition (hemoglobin/bilirubin concentration and oxygen saturation).

References
1. N. Bosschaart, M.C.G. Aalders, D.J. Faber, J.J.A. Weda, M.J.C. van Gemert, T.G. van Leeuwen, "Quantitative measurements of absorption spectra in scattering media by low-coherence spectroscopy", *Optics Letters* **34**, 3746-3748 (2009)

2. N. Bosschaart, D.J. Faber, T.G. van Leeuwen, M.C.G Aalders, "Measurements of wavelength dependent scattering and backscattering coefficients by low-coherence spectroscopy", *Journal of Biomedical Optics*, **16**, 030503 (2011)

3. N. Bosschaart, D.J. Faber, T.G. van Leeuwen, M.C.G Aalders, "*In vivo* low-coherence spectroscopic measurements of local hemoglobin absorption spectra in human skin" *Journal of Biomedical Optics* **16**, 100504 (2011)

4. R. Leitgeb, C. K. Hitzenberger, and A. F. Fercher, "Performance of fourier domain vs. time domain optical coherence tomography", *Optics Express* **11**, 889-894 (2003)

5. D.J. Faber, T.G. van Leeuwen, "Optical coherence tomography", Chapter 18 in *Optical-Thermal Response of Laser-Irradiated Tissue*, A.J. Welch, M.J.C. van Gemert, Eds., pp. 713 - 741 (Springer Science + Business Media B.V., 2010)

6. F. Robles, R.N. Graf, A. Wax, "Dual window method for processing spectroscopic optical coherence tomography signals with simultaneously high spectral and temporal resolution", *Optics Express* **17**, 6799-6812 (2009)

7. F.E. Robles, C. Wilson, G. Grant, A. Wax, "Molecular imaging true-colour spectroscopic optical coherence tomography", *Nature Photonics*, doi:10.1038/nphoton.2011.257 (2011)

8. D.J. Faber, T.G. van Leeuwen, "Doppler calibration method for spectral domain OCT spectrometers", *Journal of Biophotonics* **2**, 407-415 (2009)

9. M. Sarunic, M.A. Choma, C. Yang, J.A. Izatt, "Instantaneous complex conjugate resolved spectral domain and swept-source OCT using 3x3 fiber couplers", *Optics Express* **13**, 957-967 (2005)

10. J. Zhang, J.S. Nelson, Z. Chen, "Removal of a mirror image and enhancement of the signal-to-noise ratio in Fourier-domain optical coherence tomography using an electro-optic phase modulator", *Optics Letters* **30**, 147-149 (2005)

11. N. Nassif, B. Cense, B. Park, M. Pierce, S. Yun, B. Bouma, G. Tearney, T. Chen, J. de Boer, "In vivo high-resolution video-rate spectral-domain optical coherence tomography of the human retina and optic nerve", *Optics Express* **12**, 367-376 (2004)

12. Data tabulated from various sources compiled by S. Prahl, http://omlc.ogi.edu/spectra